ACS Catalysis

Research Article

pubs.acs.org/acscatalysis

Real Time Indirect Nanoplasmonic in Situ Spectroscopy of Catalyst Nanoparticle Sintering

Elin M. Larsson,*[,†,§,⊥] Julien Millet,[†] Stefan Gustafsson,[‡] Magnus Skoglundh,[§] Vladimir P. Zhdanov,[†,∥] and Christoph Langhammer*[,†,⊥]

[†]Division of Chemical Physics, [‡]Division of Microscopy and Microanalysis, Department of Applied Physics, and [§]Competence Center for Catalysis, Chalmers University of Technology, 412 96 Göteborg, Sweden

[⊥]Insplorion AB, Stena Center 1C, 412 96 Göteborg, Sweden

[∥]Boreskov Institute of Catalysis, Russian Academy of Sciences, Novosibirsk 630090, Russia

Supporting Information

ABSTRACT: Catalyst deactivation by sintering significantly reduces productivity and energy efficiency of the chemical industry and the effectiveness of environmental cleanup processes. It also hampers the introduction of novel energy conversion devices such as fuel cells. The use of experimental techniques that allow the scrutiny of sintering in situ at high temperatures and pressures in reactive environments is a key to alleviate this situation. Today, such techniques are, however, lacking. Here, we demonstrate by monitoring the sintering kinetics of a Pt/SiO_2 model catalyst under such conditions in real time that indirect nanoplasmonic sensing (INPS) has the potential to fill this gap. Specifically, we show an unambiguous correlation between the optical response of the INPS sensor and catalyst sintering. The obtained data are analyzed by means of a kinetic model accounting for the particle-size-dependent activation energy of the Pt detachment. Ostwald ripening is identified as the main sintering mechanism.

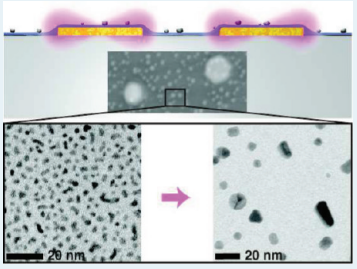

KEYWORDS: *catalyst sintering, platinum, indirect nanoplasmonic sensing, plasmon resonance, sintering kinetics, Ostwald ripening, in situ spectroscopy*

1. INTRODUCTION

Metal nanoparticles dispersed on high-surface-area support materials are widely used as highly efficient catalysts in chemical synthesis, energy conversion, and environmental cleanup applications.[1] The excess surface energy due to the high surface area of such nanoparticles makes them, unfortunately, metastable with respect to coarsening upon thermal activation.[2−6] This process, commonly referred to as *catalyst sintering*, is a major cause of catalyst deactivation, which yearly causes billions of dollars of extra cost associated with catalyst regeneration and renewal. Catalyst sintering also has a severe impact on the environment by, for example, deteriorating exhaust-cleaning catalysts in vehicles and increasing the use of raw materials and energy. Furthermore, catalyst sintering is one major reason for serious lifetime problems of fuel cells and has hitherto hampered their successful implementation.[7] Therefore, a detailed understanding of the kinetics and mechanisms of catalyst sintering under realistic application conditions in situ is of great economic, societal, and environmental importance and has a wide-ranging impact because it can pave the way for the development of strategies to minimize detrimental sintering effects. In addition, the analysis and understanding of sintering in general is of high interest for various other branches of modern technologies and related research areas of materials science, surface science, nanotechnology, and chemistry.

Mechanistically, sintering of supported metal nanoparticles includes mass transport and may occur via two widely accepted generic mechanisms:[5,6] (i) Ostwald ripening or atomic migration, in which atomic species (metal atoms alone or in the oxidized form), which are emitted from one catalyst nanoparticle, are transported and attached to another particle via surface diffusion or via the gas phase[8−11] and (ii) particle migration and coalescence,[12−14] in which entire catalyst nanoparticles diffuse over the support material until they eventually collide and coalesce.

Because of its significant practical importance, the sintering of supported metal nanoparticles has been extensively explored for several decades (see, e.g., reviews in refs 5 and15 and recent studies in refs 16−24 and references therein). The corresponding results are, however, contradictory and often controversial. The key factor behind this state of the art is that experimental studies have been and still are severely hampered by a lack of experimental techniques that allow the scrutiny of such process in situ, in real time with high resolution, and under realistic catalyst operation conditions, that is, at high temperatures (hundreds to thousands of degrees) and pressures (from atmospheric up to several hundred bar) in reactive gas

Received: November 10, 2011
Revised: December 28, 2011
Published: January 3, 2012

atmospheres. The harsh environment rules out commonly used sensitive probes such as electrons and restricts investigations to post-mortem analysis or far-from-realistic application conditions, which relates to the well-known "materials and pressure gaps" in catalysis. Recent advances made with in situ transmission electron microscopy (TEM)[17,22,23] are to be noted here as a very promising and important step into the direction outlined above. Such experiments can be performed using real reactant compositions at high temperatures but are, however, several orders of magnitude away from real reaction conditions with respect to pressure, since they typically are carried out at an upper pressure limit of ~10 mbar. Furthermore, so-called "beam effects" are often an issue, which may give rise to undesirable artifacts.

In this article, using Pt/SiO_2 as the model catalyst, we demonstrate a novel and generic experimental approach, indirect nanoplasmonic sensing (INPS),[25,26] which makes it possible to scrutinize sintering kinetics of a supported catalyst in situ and in real time with superior resolution, at short and long time scales, and in real or at realistic catalyst operation conditions. INPS uses a simple and robust experimental setup and platform (optical transmission measurement through a nanofabricated sensor chip) based on recent advances in nanoplasmonics, which generates highly relevant and novel real time data with high resolution at low cost and with high throughput. This is important to bear in mind when comparing the technique, for example, with recent in situ/environmental TEM or synchrotron/X-ray approaches. In addition, the optical INPS readout does not affect sintering kinetics, as may be the case with, for example, beam electrons.

Specifically, we show an unambiguous linear correlation between the optical response of the INPS sensor and catalyst particle density, which can be translated into an average particle diameter by means of parallel TEM image analysis and scrutiny of particle size distributions (PSDs). The so-obtained sintering kinetics are further analyzed and quantified by a kinetic model implying Ostwald ripening with the detachment activation energy dependent on the particle size (the role of the latter factor was previously articulated by Campbell et al.[9,16]). The calculations yield excellent agreement with the experimental kinetics and clearly indicate a predominantly Ostwald ripening controlled sintering mechanism, in line with recent in situ TEM studies of the same system performed at 10 mbar but under otherwise (almost) identical reaction conditions.[22,23] Thus, our work provides a general blueprint for real time in situ sintering studies which, in combination with optical nanocalorimetry,[25] have the potential to become a unique (spectroscopic) tool for in operando[27] studies. In this work, INPS is used at atmospheric pressure in reactive gas environment and up to 610 °C. INPS experiments at higher pressures and temperatures are also possible but require a modified reactor design.

2. EXPERIMENTAL SECTION

General Considerations. The principle of INPS is so-called nanoplasmonic sensing (localized surface plasmon resonance, LSPR).[28] The latter guarantees a remote readout, making measurements at high temperatures and pressures easily possible. In particular, INPS utilizes the LSPR excitation in gold sensor nanoparticles fabricated onto a generic sensor chip to study processes and changes on/in *adjacent* functional nanomaterials (i.e., physically separated from the Au sensor by a spacer layer which, in the present case, mimics the support material of a real catalyst) through the coupling of the locally enhanced plasmonic field to the latter or through the intrinsic temperature sensitivity of the LSPR (optical nanocalorimetry).[25] In general, the INPS principle can be used to quantitatively study physical and chemical properties and processes involving metallic and nonmetallic nanostructures at the ensemble[25,26,29] and (by utilizing modified sensor structure designs) at the single particle level.[30,31] In the particular case considered here, simply speaking, the rearrangement of the Pt nanoparticles on the sensor during sintering induces a change in the local dielectric environment of the sensor, which is reflected in and read out as a spectral shift of the Au gold sensor nanoparticle LSPR peak.

The sensor chips used here consist of the INPS sensing structure and the catalyst as schematically illustrated in Figure 1a. The sensor consists of plasmonic gold nanodisks (average diameter 80 nm, height 20 nm) deposited on a glass slide and covered by a 10 nm thick SiO_2 spacer layer onto which the Pt model catalyst is deposited. The spacer layer serves several functions, including (i) protection of the Au nanodisks from the environment and from structural reshaping, (ii) providing tailored surface chemistry (i.e., catalyst support material) for the material/catalyst to be studied, and (iii) preventing the catalyst from directly interacting with the Au nanodisks by, for example, alloy formation. In principle, any other dielectric material, which can be deposited as a thin flat or porous film, such as TiO_2 or Al_2O_3, can be used as a spacer layer.

INPS Sensor Chip Nanofabrication. To make the INPS sensor chips, Au nanodisks (diameter = 80 nm, height = 20 nm) were fabricated on borofloat glass substrates using hole-mask colloidal lithography.[37] A heat treatment (615 °C for 3 h in air) of the Au nanodisks was used to obtain a thermally (in the temperature range of the experiments) stable particle shape. Subsequently, a thin (thickness l = 10 nm) SiO_2 layer was deposited onto the chip using sputtering. The SiO_2 layer was thermally stabilized using a 36 h heat treatment at 615 °C (in air) before depositing the platinum catalyst nanoparticles. The latter were deposited by thermally (electron beam evaporation, 0.05 nm/s) evaporating a thin granular platinum film with nominal thickness of 0.5 nm.

Experimental Setup for Sintering Kinetics Measurements. The experiments were performed in an Insplorion X1 gas flow reactor (Insplorion AB, Göteborg, Sweden, www.insplorion.com). A gas flow rate of 16.7 mL/s (plug flow velocity 3.4 cm/s) was used, and the chamber was kept at atmospheric pressure. Optical spectra were collected using an array spectrometer and analyzed for the LSPR centroid position[32] employing Insplorer software (subsecond time resolution). Before each experiment, the temperature was increased in Ar (4.5 purity) to the one desired for the sintering measurements and kept at this level for 30 min to stabilize reactor temperature. No or almost no sintering was observed in Ar at the temperatures used here (≤615 °C). Sintering of the Pt nanoparticles was then induced by changing the gas feed to 4% O_2 in Ar at the designated temperature. To prevent further sintering after the desired time interval, TEM samples were cooled to room temperature in 100% Ar.

ESEM Imaging. An ESEM (FEI Quanta 200 ESEM FEG) was used to take images of an INPS sensor chip before and after (ex situ) sintering in the Insplorion X1. An acceleration voltage of 20 keV and 0.75 Torr water vapor was used during imaging to neutralize charging as typical for samples with non-conductive substrate (glass).

dx.doi.org/10.1021/cs200583u | ACS Catal. 2012, 2, 238–245

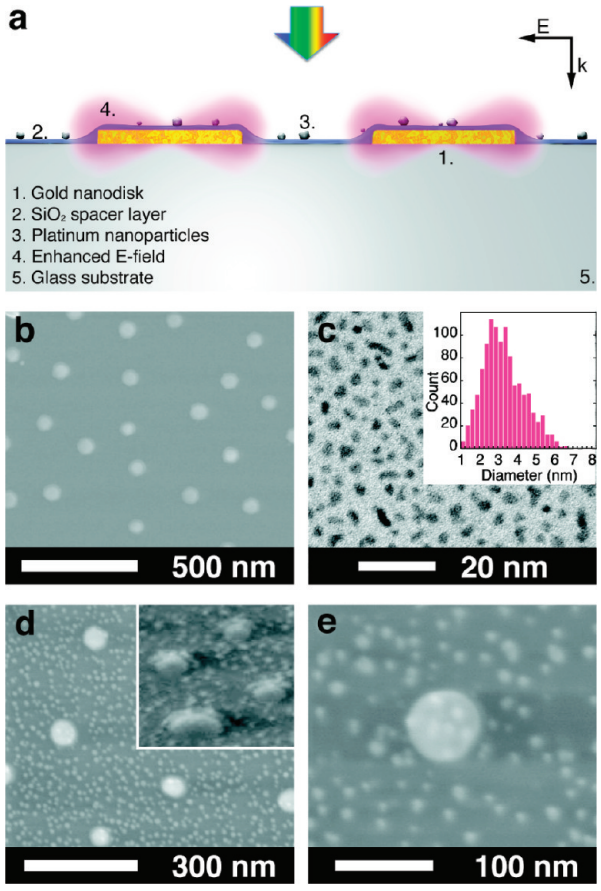

Figure 1. Indirect nanoplasmonic sensing (INPS) platform for *in situ* sintering studies. (a) Schematic depiction of the cross-section of the used INPS sensor. The sensing structure consists of an array of gold nanodisks (average diameter = 80 nm, height = 20 nm) deposited on a conventional glass slide and covered by a 10 nm thick SiO_2 spacer layer onto which the Pt model catalyst particles were deposited through thermal evaporation. (b) ESEM image of a sensor surface *prior to* the sintering experiment. No Pt particles can be resolved. (c) TEM micrograph of the initial "as deposited" Pt nanoparticles on the sensor surface prior to heating/sintering. The inset shows the corresponding PSD yielding an average particle diameter of 3.3 ± 1.1 nm. (d) ESEM image of a sensor surface *after* a 6 h sintering experiment in 4% O_2 at 610 °C. Clearly, the sintered Pt catalyst particles are now resolved. The inset comprises a tilted (60°) ESEM image of the same sample surface as in the larger image. The SiO_2 spacer layer is clearly visible as well as the gold nanodisks and the Pt model catalyst. (e) ESEM picture of a single Au sensor nanodisk on the same sample as shown in panel (d). The sintered Pt catalyst particles are clearly visible both in the close vicinity and on the surface of the Au sensor.

TEM Imaging and Analysis. Samples for TEM imaging were prepared on silicon nitride TEM windows[38] by deposition of a 10 nm SiO_2 film by sputtering, followed by a 0.5 nm thick granular platinum film to mimic the structure on the INPS chips. Typically, the materials were deposited during the same process as the corresponding INPS samples for maximal comparability. The TEM window samples were, subsequently, inserted into the Insplorion X1 and exposed to the same gas and temperature conditions as the INPS samples. The TEM imaging was then, post mortem, carried out in a Philips CM200 FEG 200 TEM at 200 keV acceleration voltage. ImageJ analysis software was used for image analysis to obtain particle diameter, particle density, and surface coverage.

3. RESULTS

As demonstrator, we here use the sintering of Pt nanoparticles formed via the (electron beam) evaporation of a granular film of nominal thickness 0.5 nm onto the sensor. The amount of Pt is sufficiently low so that individual Pt nanoparticles with an average diameter of $\langle D \rangle$ = 3.3 nm (±1.1 nm) are formed (Figure 1c), which mimics the size range of real supported catalysts. Figure 1b shows an environmental scanning electron microscopy (ESEM) image of a sensor chip with Au nanodisks, SiO_2 spacer layer, and Pt nanoparticles before any sintering has occurred. At this stage, the Pt particles are too small to be resolved by ESEM, and only the Au nanodisks are seen in the image. Figure 1c shows a TEM micrograph and the corresponding PSD of Pt nanoparticles "as deposited" before any sintering or reshaping due to heating have occurred. The TEM image was obtained from a TEM window sample prepared in parallel with the INPS sample, but without the Au nanodisks. An ESEM micrograph of the same INPS sample as in Figure 1b after 6 h sintering at 610 °C in 4% O_2 in Ar is shown in Figure 1d. Because of the significant sintering of the Pt nanoparticles that has occurred, they are now clearly resolved. The inset comprises a tilted ESEM image of the same surface where the SiO_2 spacer layer is clearly visible. Figure 1e, finally, displays an ESEM micrograph of a single Au sensor nanodisk where the sintered Pt catalyst particles are visible both in the close vicinity and on the surface of the Au sensor.

To demonstrate the applicability of INPS for in situ monitoring of model catalyst sintering, experiments were performed in which the LSPR centroid wavelength, $\Delta\lambda$, (i.e., the center of mass of the top part of the peak following the procedure by Dahlin et al.[32]) was monitored during Pt nanoparticle sintering at different temperatures in an inert (Ar) or oxidizing (4% O_2 in Ar) environment at atmospheric pressure. TEM samples, prepared as above, were run in parallel with the optical measurements and were imaged and analyzed for particle size, number density, and surface coverage.

Figure 2a shows the optical absorbance spectra obtained at different time intervals during the sintering of Pt nanoparticles in 4% O_2 (in Ar) at 610 °C. We note that the temperature was allowed to stabilize for 30 min in inert Ar atmosphere before the onset of the experiments, that is, addition of O_2 to the feed. Clearly, as the Pt nanoparticles undergo significant sintering, the LSPR peak shifts toward shorter wavelengths and, simultaneously, a decrease in the optical absorbance is observed. Analysis of $\Delta\lambda$ during the course of the experiment in real time shows that the LSPR shifts fast in the beginning and then more slowly toward the end of the experiment (black curve Figure 2b). In contrast, when the same experiment is performed in pure Ar (or, as a control experiment displayed in Figure S1 in the Supporting Information, in 4% O_2/Ar on a "blank" sensor without Pt) no significant shift during the entire experiment is observed. The latter is a strong indicator that the measured LSPR peak shift is directly related to the sintering of the Pt particles, in particular, since O_2 is a well-known sintering promoter for Pt.[33]

This prediction made on the basis of the INPS signal is directly confirmed by the TEM analysis of the Pt particles after 5 min and 6 h in 4% O_2/Ar and Ar, respectively, shown in Figure 2c–f. Exposure of the Pt nanoparticles to Ar at 610 °C resulted in the transformation of the irregular shapes of the as-prepared particles to predominantly circular projected shapes (Figure 2c), with a fairly narrow PSD ($\langle D \rangle$ = 3.12 ± 0.8 nm). A

dx.doi.org/10.1021/cs200583u | ACS Catal. 2012, 2, 238–245

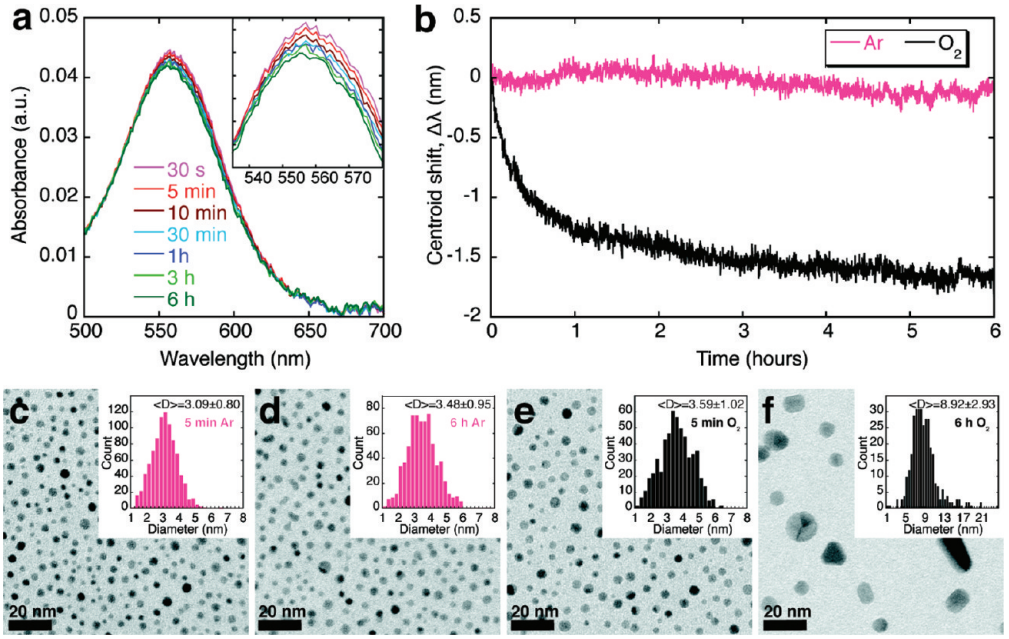

Figure 2. INPS sensor response to model catalyst sintering: real time kinetics and TEM. (a) Absorbance spectra obtained at different times during the sintering of the Pt model catalyst in 4% O_2/Ar at 610 °C. The LSPR peak of the INPS sensor spectrally shifts to the blue, and simultaneously, a decrease in the optical absorbance is observed. (b) Diagram showing the LSPR peak centroid shift vs sintering time in 4% O_2/Ar (black) and 100% Ar (pink) atmosphere. Clearly, in O_2, which is known to promote the sintering of supported Pt catalysts, the centroid shifts fast in the beginning and then more slowly, almost linearly, toward the end. In contrast, in pure Ar, only a very small centroid shift is seen. TEM pictures and corresponding PSD histograms of the Pt nanoparticles after 5 min (c) and 6 h (d) in pure Ar at 610 °C reveal an almost constant particle size, indicating almost total absence of sintering. TEM images and PSD histograms after 5 min (e) and 6 h (f) in 4% O_2/Ar at 610 °C clearly show significant Pt catalyst particle sintering, in agreement with the INPS sintering kinetic curve.

circular projected shape reflects a compact three-dimensional nanoparticle shape consistent with surface energy minimization. To obtain $\langle D \rangle$, a spherical shape is assumed. Slow sintering is observed in Ar at this temperature, causing $\langle D \rangle$ to increase from 3.12 to 3.48 nm after 6 h; however, already after 5 min in 4% O_2/Ar, the Pt nanoparticles have sintered more than after 6 h in Ar and after 6 h sintering in O_2, $\langle D \rangle$ has increased up to 8.9 nm.

At this point, it is also important to consider other potential effects that could give rise to a spectral shift of the Au nanodisk LSPR in a sintering experiment as performed here. For example, the sudden exposure of the sensor to 4% O_2 to induce sintering leads to the adsorption of oxygen onto the Pt particles and (chemical interaction with) the sensor, which, by itself, induces a spectral shift. The latter is, however more or less instantaneous and therefore gives rise to a sharp step in the $\Delta\lambda$-vs-t curve in the first seconds of the experiment. Consequently, it basically does not interfere with the sintering kinetics signal, which is a process that takes place on much longer time scales. This behavior was verified in control experiments (not shown) in which the sintering process at 600 °C in 4% O_2 was interrupted by numerous 30 min steps in pure Ar, showing an immediate and reversible response of the sensor to O_2 adsorption and desorption (identical in magnitude for each cycle) superimposed over a continuous, slower, and irreversible red shift stemming from the sintering of the Pt nanoparticles. The identical magnitude of the oxygen adsorption steps for each cycle also clearly shows that the LSPR signal is not influenced by (potential) changes in the oxygen coverage on the Pt particles (caused by particle size growth).

To further demonstrate the direct correlation between the plasmonic signal from the INPS sensor and sintering of Pt nanoparticles, experiments were performed in which the sintering process was interrupted after different exposure times of the samples to 4% O_2/Ar atmosphere at 550 °C (Figure 3a). TEM imaging was performed intermittently after each sintering time interval. The TEM images together with corresponding PSDs are shown in Figure 3b–g. Plotting $\Delta\lambda$ as a function of sintering time for the six different experiments (t = 10 min, 30 min, 1 h, 3 h, 6 h, and 12 h) in Figure 3a shows, as a first general observation, that the signal is completely reproducible during overlapping sintering intervals for different samples. The latter demonstrates the robustness and reproducibility of the INPS approach.

A closer inspection of the TEM micrographs and corresponding PSDs reveals two significantly different regimes. In the first regime, which extends from the start of the experiment to somewhere between 2 and 3 h, the initial Gaussian PSD is transformed into a log-normal distribution. Interestingly, in a second regime after 3 h of sintering, a gradually more pronounced shoulder of significantly larger particles appears and starts to grow in the PSD, which after 12 h has turned into a more bimodal-like distribution. The appearance of such "unexpectedly large" particles has been observed previously.[2,34] The underlying mechanism is, to date, still debated.

Sintering kinetics obtained at 450, 500, and 550 °C for a 2 h interval of exposure to 4% O_2/Ar are shown in Figure 4a. Clearly, smaller $\Delta\lambda$'s, indicating less sintering, are found at lower temperatures. The latter is confirmed by the analysis of the corresponding TEM micrographs and PSDs (Figure 4b–d).

To analyze and quantify the sintering kinetics measured with INPS, we need to correlate the optical response, that is, the centroid shift $\Delta\lambda$, with the structural/size changes of the

dx.doi.org/10.1021/cs200583u | ACS Catal. 2012, 2, 238–245

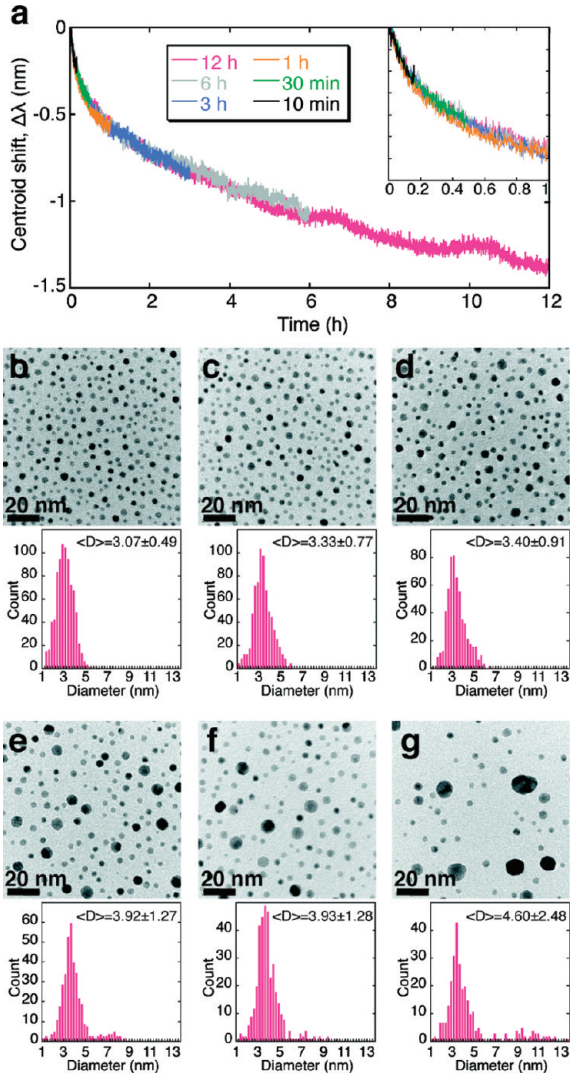

Figure 3. Step-wise sintering kinetics and TEM analysis at 550 °C. (a) Real time plasmonic sintering kinetic curves obtained for six different samples and sintering times under identical experimental conditions (4% O_2/Ar atmosphere at 550 °C) demonstrate striking reproducibility between experiments and illustrate the robustness of the INPS platform. Corresponding TEM micrographs obtained after each sintering time interval; that is, 10 min (b), 30 min (c), 1 h (d), 3 h (e), 6 h (f), and 12 h (g), with respective PSD histograms and average particle diameters ⟨D⟩ clearly illustrate the significant sintering of the Pt model catalyst, as registered by the INPS sensor. Note the appearance of a bimodal-like PSD for longer sintering times.

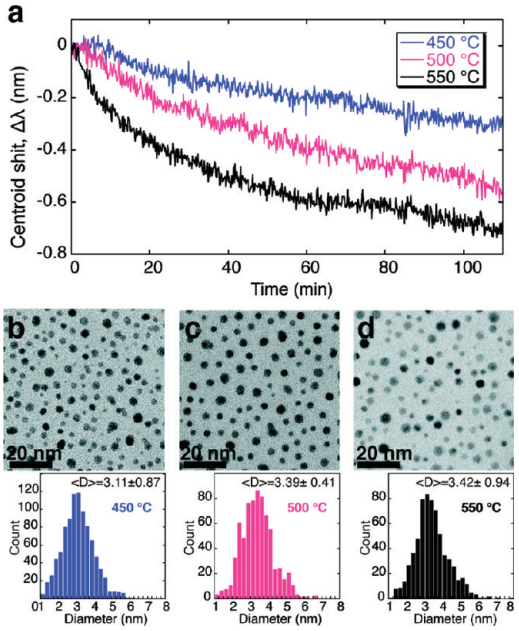

Figure 4. Sintering kinetics and TEM for different temperatures. (a) Real time plasmonic sintering kinetic curves obtained at three different temperatures in 4% O_2/Ar atmosphere during 2 h exposure. Clearly, the sintering rate decreases with decreasing temperature. TEM micrographs and corresponding PSDs obtained after two hours of sintering at (b) 450, (c) 500, and (d) 550 °C confirm the reduced sintering rate for decreasing temperature, as predicted by the kinetic curves.

catalyst particles during the sintering process. In Figure 5a, $\Delta\lambda$ values from the sintering experiments (Figures 2–4) are plotted versus the Pt particle density P on the sensor surface, as obtained from TEM image analysis (discrete symbols). Clearly, a direct linear correlation between the two parameters is found, yielding an empirical "calibration function" by linear regression analysis: $\Delta\lambda = -1.71 + (5.69 \times 10^{-5})P$ (with an R value of 0.96 for the fit) where P is the particle density (μm^{-2}) and $\Delta\lambda$ is the centroid shift (nm). We note that the three measurement series in Figure 5a were performed using three different sample batches, yielding slightly different starting conditions for the experiments, which most likely is the main reason for the small discrepancies between the series.

For further quantitative analysis of the obtained sintering kinetics, it is desirable to have a correlation of $\Delta\lambda$ with catalyst particle size D. The PSDs for the systems studied here are, however, not symmetrical, with the longest sintering times at 550 °C as the most extreme case (bimodal PSD), and it is not obvious how to calculate a physically relevant D to correlate with. It is possible, however, to derive D from the nominal thickness of the evaporated Pt film and the linear particle density calibration function obtained in Figure 5a, assuming that the total Pt volume is preserved. The latter assumption is verified by back-calculating the nominal thickness of the evaporated Pt film from particle diameters obtained from TEM image analysis and included in the PSDs. The validity of this assumption is also clearly seen in Figure 5b, showing that the particle surface coverage S (as obtained from TEM image analysis) is proportional to P as $S = 0.67P^{0.34}$ (with an R value of 0.99 for the fit) which is, as expected, in good agreement with the analytically predicted correlation of $S \propto P^{1/3}$ for constant volume and spherical particles. Consequently, the *calculated* particle diameter, D_P, obtained by relying on our calibration function can be directly correlated with $\Delta\lambda$. The so-obtained empirical relation reads as $D_P = 2000[(8.53 \times 10^{-8})/(4\pi\cdot(\Delta\lambda + 1.71))]^{1/3}$, where D_P is expressed in nanometers and $\Delta\lambda$ is the centroid shift (also in nanometers).

The relation introduced above represents a "universal calibration function" for the studied system, relating $\Delta\lambda$ to D_P, which corresponds to the PSD as weighted by the INPS sensor. Using this calibration, $\Delta\lambda$ can be translated into an average particle diameter to obtain real-time sintering kinetics with high temporal resolution (we note that the *absolute* $\Delta\lambda$ value obtained per change in D_P depends on the number density of the Pt particles at the starting point of the sintering

dx.doi.org/10.1021/cs200583u | *ACS Catal.* 2012, 2, 238–245

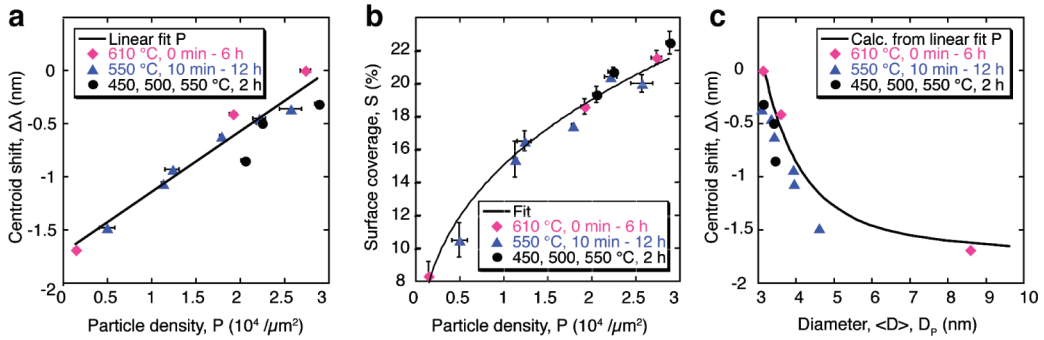

Figure 5. Correlations between plasmonic response and sintered particle structure/size. (a) Centroid shift $\Delta\lambda$ versus the Pt particle density, P, on the sensor surface, as obtained from TEM image analysis for the three measurement series presented above (discrete symbols). Error bars show standard deviation. The black solid line corresponds to a linear regression fit yielding an empirical calibration curve: $\Delta\lambda = -1.71 + (5.69 \times 10^{-5})P$. (b) Particle surface coverage, S (as obtained from TEM image analysis), versus P yielding the correlation $S = 0.67 \cdot P^{0.34}$. The latter is in agreement with the analytically predicted correlation of $S \propto P^{1/3}$ for constant volume and spherical particles. (c) The black solid line corresponds to the calculated particle diameter, D_P, derived from the particle density calibration curve obtained in part a by assuming a preservation of the total Pt volume on the surface and spherical particles (as confirmed in part b). It yields the empirical relation: $D_P = 2000[(8.53 \times 10^{-8})/(4\pi(\Delta\lambda + 1.71))]^{1/3}$. The discrete symbols represent the arithmetic mean particle diameters, $\langle D \rangle$, as obtained from TEM images. Clearly, both D_P and $\langle D \rangle$, show a nonlinearly decreasing centroid response for increasing particle size, that is, for the longer sintering times. For all three panels, we note that the three measurement series were obtained from three different sample batches, which is the main reason for the small discrepancies.

experiment; that is, that a new calibration function has to be established for a new experimental system with different initial Pt (or other metal) nanoparticle loading/dispersion/number density on the sensor).

For comparison, the discrete symbols in Figure 5c represent the arithmetic mean particle diameters, $\langle D \rangle$, as obtained from the TEM images shown above. Clearly, both particle size parameters, D_P and $\langle D \rangle$, show a nonlinearly decreasing $\Delta\lambda$ response for increasing particle size, that is, for the longer sintering times. We note, however, that in the 550 °C data set for $t > 3$ h, the relatively low number of large particles (containing, however, almost 2/3 of the total volume) are underrepresented in $\langle D \rangle$ compared to D_P, which is the reason for the deviation of $\langle D \rangle$ from the D_P curve in that range. Furthermore, it is also important to generally note that a single parameter, such as D_P or $\langle D \rangle$, only to a certain approximation describes a PSD (in particular, an asymmetric one) and that relevant information about the sintering mechanism contained in the shape of the PSD may be lost. As a consequence, some caution must be taken when using D_P or $\langle D \rangle$ as the sole descriptor of sintering kinetics.

4. DISCUSSION

Because of the superior temporal resolution and in situ measurement capability at ambient/high gas pressure, the INPS sintering kinetics described above are more detailed than those obtained by other techniques (the latter kinetics often contain only a few data points or, as temperature-programmed low energy ion scattering (TP-LEIS) spectroscopy data, may have similar time resolution but cannot be obtained in situ under ambient/high gas pressures) and thus more suitable for curve-fitting. To show our corresponding results in a historical context, we recall that the growth of the average particle radius is often asymptotically described by a power law, $\langle R \rangle \propto t^{1/n}$, where n is the exponent dependent on the sintering mechanism. For Ostwald ripening with 2D detachment, diffusion, and attachment, the conventional models[8−11] based on the classical Lifshitz−Slyozov−Wagner (LSW) theory,[35,36] predict $n = 3$ and 4 for kinetically and diffusion-limited growth, respectively. For particle migration and coalescence, n is expected[12−14] to be between 5 and 7. The experiments, performed in the past, often reported that n is comparable to or larger than the latter values (reviewed by Bartholomew[5]). Finally, particle growth with $n = 2$ was recently observed for the Pd/Al_2O_3 system.[24]

Formally, the power-law growth can be derived using the phenomenological power-law equation, $d\langle R \rangle/dt = A/\langle R \rangle^{n-1}$, where A is the parameter describing the Arrhenius dependence of the rate of the process resulting in sintering. This equation has been validated by the conventional LSW-type models as well as by analytical and Monte Carlo results obtained assuming the sintering to occur via nanoparticle migration. In our case, the use of this equation to fit the experimental kinetics yields $n = 5$ (see the Supporting Information). This exponent is larger than those ($n = 3$ or 4) predicted for 2D Ostwald ripening by the LSW-type models, and accordingly, it could be interpreted as the process occurring via nanoparticle diffusion (which, however, contradicts recent results[22−24]).

Alternatively, we have employed the kinetic equation taking into account that the activation energy for Pt detachment resulting in Ostwald ripening depends on the particle radius due to surface tension, γ (see the Supporting Information). Specifically, the corresponding contribution has been phenomenologically described as $\Delta E = -2\gamma\upsilon/k_B TR$, where υ is the atomic volume, and R is the particle radius (a more accurate expression should take the details of the structure of nanoparticles into account;[9,10,16] however, the corresponding formulas applicable for our particles, which are covered by oxygen, are lacking). Following this line, our experimental kinetics can now be accurately fitted (Figure 6) using $n = 3$ and physically reasonable parameters (the size-independent part of the detachment activation energy is, for example, found to be 364 kJ/mol, whereas the surface energy is 1.5 J/m^2). The obtained exponent, $n = 3$, clearly indicates that Ostwald ripening is the dominant sintering mechanism, that is, that there is no or almost no diffusion of Pt nanoparticles. This finding is in agreement with the recent in situ TEM studies[23] of the sintering of Pt nanoparticles under similar sintering conditions on SiO_2 support, fabricated using the same deposition systems as used in this work.

dx.doi.org/10.1021/cs200583u | ACS Catal. 2012, 2, 238−245

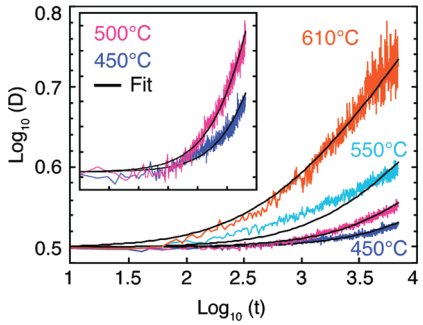

Figure 6. Quantitative analysis of INPS sintering kinetics. The solid black lines show calculated fits to the experimentally obtained dependence of the particle diameter, D (measured in nanometers); on time, t (measured in seconds); assuming the sintering to occur via 2D kinetically limited Ostwald ripening and taking into account that the Pt detachment activation energy depends on the nanoparticle diameter. With $n = 3$, the agreement is nearly perfect for 450, 500, and 610 °C, whereas for 550 °C, the agreement is worse. The likely reason is deviation of the PSD from the monodisperse form, as discussed in the text.

We note at this point that the presented fits to our experimental data imply that the PSDs during the sintering process are self-similar. As seen clearly from the TEM images presented above, this assumption is valid provided that the sintering time is not too long. For this reason, the analysis is shown for a relatively short time interval only (up to the first 2 h) where the PSDs indeed are narrow and relatively symmetric.

In the above context, it is also of interest to discuss the case of 550 °C (Figure 6) in more detail, since the corresponding fit is of poorer quality compared with the others. This implies (i) a different sintering mechanism, (ii) a problem with our conversion of $\Delta\lambda$ into particle size for this temperature, or both. As indicated, to solely describe a PSD by a single parameter such as $\langle D \rangle$ or D_p is a significant simplification. Thus, bearing in mind the rather asymmetric/bimodal PSD observed for the 550 °C case with the appearance of unexpectedly large particles, it is not surprising that the fit is not as good as for the other cases in which the PSD is basically self-similar. In fact, this deviation also nicely illustrates how, thanks to the superior resolution of INPS, details in the sintering kinetics as those at 550 °C can be clearly (i) identified and (ii) related to peculiarities in the PSD, which, in combination, allow conclusions about the sintering mechanism. For the case of 550 °C, the mechanism appears to be more complex than at the other temperatures investigated here and will be the subject of further, more detailed, investigation.

In summary, INPS constitutes an experimental platform with the potential to significantly alleviate the lack of robust and versatile experimental techniques to scrutinize the sintering of heterogeneous catalysts in situ under application conditions, and accordingly, it may have a profound significance for the detailed understanding of catalyst sintering kinetics and mechanisms and for the development of more sintering-resistant catalyst systems. Specifically, we have demonstrated the unambiguous direct correlation of the optical response, that is, the centroid shift, $\Delta\lambda$, of the LSPR peak of INPS sensors with sintering by intermittent TEM imaging and PSD analysis. Utilizing the identified correlations, the sintering kinetics measured in situ with a temporal resolution in the subsecond range were successfully analyzed by a physically suitable kinetic model. Owing to the superior resolution of the obtained kinetics, deeper conclusions about the sintering mechanism could be made than would have been possible by only intermittent TEM imaging. In particular, we show by fitting our kinetics that the particle-size dependence of the activation energy for Pt-species detachment from nanoparticles is crucial for the interpretation of nanoparticle sintering kinetics and that Ostwald ripening is the governing sintering mechanism. In our work, this dependence was represented by using the conventional phenomenological expression for the detachment activation energy. Despite its simplicity, this expression correctly describes the scale of the effect.

Finally, we note that the presentation of our work has primarily been framed in the context of heterogeneous catalysis. In a wider perspective, however, the analysis and understanding of sintering kinetics and mechanisms, in general, which becomes possible with INPS, is of high interest also in various other research areas, including materials science, surface science, nanotechnology, and chemistry.

■ ASSOCIATED CONTENT

Ⓢ Supporting Information

Detailed derivation of the sintering kinetics modeling. A control experiment in which a blank INPS sensor (i.e., Au nanoparticles, covered by a SiO_2 layer, without Pt nanoparticles) is exposed to oxidizing atmosphere as during a sintering experiment. This material is available free of charge via the Internet at http://pubs.acs.org.

■ AUTHOR INFORMATION

Corresponding Author

*E-mails: (E.M.L.) elarsson@chalmers.se, (C.L.) clangham@chalmers.se

■ ACKNOWLEDGMENTS

We acknowledge financial support from the Swedish Research Council project 2010-4041 "Nanoplasmonics for Nanomaterials Science"; the Swedish Energy Agency (STEM) projekt dnr. 0189-1; "Nanoscience and Nanotechnology for Sustainable Energy and Environment (NANO-SEE)"; EMRP researcher grant no. IND15-REG1; and from the Competence Centre for Catalysis, which is financially supported by Chalmers University of Technology, the Swedish Energy Agency, and the member companies: AB Volvo, Volvo Car Corporation, Scania CV AB, Saab Automobile Powertrain AB, Haldor Topsøe A/S, and ECAPS AB.

■ REFERENCES

(1) Li, Y.; Somorjai, G. A. *Nano Lett.* **2010**, *10* (7), 2289−2295.
(2) Wynblatt, P. *Acta Metall.* **1976**, *24* (12), 1175−1182.
(3) Wynblatt, P.; Gjostein, N. A. *Acta Metall.* **1976**, *24* (12), 1165−1174.
(4) Fuentes, G. A.; Salinas-Rodriguez, E. In *Catalyst Deactivation*; Bartholomew, G. A., Fuentes, G. A., Eds.; Elsevier Science: Amsterdam, 1997; pp 573−583.
(5) Bartholomew, C. H. *Appl. Catal., A* **2001**, *212* (1−2), 17−60.
(6) Moulijn, J. A.; van Diepen, A. E.; Kapteijn, F. In *Handbook of Heterogeneous Catalysis*, 2 ed.; Ertl, G., Knözinger, H., Schüth, F., Weitkamp, J., Eds.; Wiley-VCH Verlag GmbH & Co. KGaA: Weinheim, 2008; Vol. *4*.
(7) Borup, R.; Meyers, J.; Pivovar, B.; Kim, Y. S.; Mukundan, R.; Garland, N.; Myers, D.; Wilson, M.; Garzon, F.; Wood, D.; Zelenay, P.; More, K.; Stroh, K.; Zawodzinski, T.; Boncella, J.; McGrath, J. E.; Inaba, M.; Miyatake, K.; Hori, M.; Ota, K.; Ogumi, Z.; Miyata, S.;

Nishikata, A.; Siroma, Z.; Uchimoto, Y.; Yasuda, K.; Kimijima, K.-i.; Iwashita, N. *Chem. Rev.* **2007**, *107* (10), 3904−3951.
(8) Wynblatt, P.; Gjostein, N. A. *Prog. Solid State Chem.* **1975**, *9*, 21−58.
(9) Parker, S. C.; Campbell, C. T. *Phys. Rev. B* **2007**, *75* (3), 035430.
(10) Houk, L. R.; Challa, S. R.; Grayson, B.; Fanson, P.; Datye, A. K. *Langmuir* **2009**, *25* (19), 11225−11227.
(11) Prevot, G. *Phys. Rev. B* **2011**, *84* (4), 045434.
(12) Ruckenstein, E.; Pulvermacher, B. *J. Catal.* **1973**, *29* (2), 224−245.
(13) Lopez, N.; Norskov, J. K.; Janssens, T. V. W.; Carlsson, A.; Puig-Molina, A.; Clausen, B. S.; Grunwaldt, J. D. *J. Catal.* **2004**, *225* (1), 86−94.
(14) Zhdanov, V. P. *Surf. Rev. Lett.* **2008**, *15* (3), 217−220.
(15) Datye, A. K.; Xu, Q.; Kharas, K. C.; McCarty, J. M. *Catal. Today* **2006**, *111* (1−2), 59−67.
(16) Campbell, C. T.; Parker, S. C.; Starr, D. E. *Science* **2002**, *298* (5594), 811−814.
(17) Hansen, P. L.; Wagner, J. B.; Helveg, S.; Rostrup-Nielsen, J. R.; Clausen, B. S.; Topsøe, H. *Science* **2002**, *15*, 2053−2055.
(18) Parker, S.; Campbell, C. *Top. Catal.* **2007**, *44* (1), 3−13.
(19) Tanabe, T.; Nagai, Y.; Dohmae, K.; Sobukawa, H.; Shinjoh, H. *J. Catal.* **2008**, *257* (1), 117−124.
(20) Yang, F.; Chen, M. S.; Goodman, D. W. *J. Phys. Chem. C* **2008**, *113* (1), 254−260.
(21) Alloyeau, D.; Prevot, G.; Le Bouar, Y.; Oikawa, T.; Langlois, C.; Loiseau, A.; Ricolleau, C. *Phys. Rev. Lett.* **2011**, *105* (25), 255901.
(22) Simonsen, S. B.; Chorkendorff, I.; Dahl, S.; Skoglundh, M.; Sehested, J.; Helveg, S. *J. Am. Chem. Soc.* **2010**, *132* (23), 7968−7975.
(23) Simonsen, S. B.; Chorkendorff, I.; Dahl, S.; Skoglundh, M.; Sehested, J.; Helveg, S. *J. Catal.* **2011**, *281* (1), 147−155.
(24) Xu, Q.; Kharas, K. C.; Croley, B. J.; Datye, A. K. *ChemCatChem* **2011**, *3* (6), 1004−1014.
(25) Langhammer, C.; Larsson, E. M.; Kasemo, B.; Zoric, I. *Nano Lett.* **2010**, *10* (9), 3529−3538.
(26) Larsson, E. M.; Langhammer, C.; Zoric, I.; Kasemo, B. *Science* **2009**, *326* (5956), 1091−1094.
(27) Banares, M. A. *Catal. Today* **2005**, *100* (1−2), 71−77.
(28) Anker, J. N.; Hall, W. P.; Lyandres, O.; Shah, N. C.; Zhao, J.; Van Duyne, R. P. *Nat. Mater.* **2008**, *7* (6), 442−453.
(29) Langhammer, C.; Zhdanov, V. P.; Zoric, I.; Kasemo, B. *Phys. Rev. Lett.* **2010**, *104* (13), 135502.
(30) Liu, N.; Tang, M. L.; Hentschel, M.; Giessen, H.; Alivisatos, A. P. *Nat. Mater.* **2011**, *10*, 631−636.
(31) Shegai, T.; Langhammer, C. *Adv. Mater.* **2011**, *23* (38), 4409−4414.
(32) Dahlin, A. B.; Tegenfeldt, J. O.; Höök, F. *Anal. Chem.* **2006**, *78* (13), 4416−4423.
(33) Chen, M.; Schmidt, L. D. *J. Catal.* **1978**, *55* (3), 348−360.
(34) Harris, P. J. F.; Boyes, E. D.; Cairns, J. A. *J. Catal.* **1983**, *82*, 127−146.
(35) Lifshitz, I. M.; Slyozov, V. V. *J. Phys. Chem. Solids* **1961**, *19*, 35−50.
(36) Wagner, C. *Z. Elektrochem.* **1961**, *65*, 581−591.
(37) Fredriksson, H.; Alaverdyan, Y.; Dmitriev, A.; Langhammer, C.; Sutherland, D. S.; Zaech, M.; Kasemo, B. *Adv. Mater.* **2007**, *19* (23), 4297−4302.
(38) Grant, A. W.; Hu, Q.-H.; Kasemo, B. *Nanotechnology* **2004**, *15* (9), 1175.